Available online at www.sciencedirect.com

ScienceDirect

Ceramics International 40 (2014) 1351–1358

CERAMICS INTERNATIONAL

www.elsevier.com/locate/ceramint

Hydrothermal synthesis, characterization and optical properties of ellipsoid shape α-Fe_2O_3 nanocrystals

Maryam Mohammadikish*

Faculty of Chemistry, Kharazmi University, Tehran, Iran

Received 23 May 2013; received in revised form 30 May 2013; accepted 2 July 2013
Available online 16 July 2013

Abstract

A facile hydrothermal method for the synthesis of α-Fe_2O_3 nanocrystals is described. The crystalline structure and morphology of the as-prepared product were investigated by using X-ray diffraction (XRD), Fourier transform infrared spectroscopy (FTIR), scanning electron microscopy (SEM) and transmission electron microscopy (TEM). Powder X-ray diffraction pattern exhibited pure rhombohedral structure. The SEM and TEM results showed that the average diameter of the highly crystalline ellipsoid shape α-Fe_2O_3 nanocrystals was about 40–50 nm. The band gap energies were investigated by the UV–vis absorption studies.

Keywords: α-Fe_2O_3; Nanocrystals; Hydrothermal; Band gap

1. Introduction

Recently, the synthesis of oxide nanoparticles have received more attention due to their unique optical, electrical and magnetic properties [1,2].

Fe_2O_3 has four phases: α-Fe_2O_3 (hematite), β-Fe_2O_3, γ-Fe_2O_3 (maghemite), and ξ-Fe_2O_3 [3]. Among them α-Fe_2O_3 has the corundum structure, while the others have the cubic structure [4]. Magnetic nanoparticles of γ-Fe_2O_3 have been used in magnetic refrigeration, information storage, controlled drug delivery, bioprocessing and ferrofluids [5,6], while α-Fe_2O_3 is of great interest for potential applications as a gas sensor, lithium ion battery, catalyst, and pigment [7–9]. The environmental friendly α-Fe_2O_3 (hematite), an n-type semiconductor (E_g=2.1 eV), is the most stable iron oxide phase under ambient conditions. It is widely used in gas sensors, catalysts, high density magnetic recording media, clinical therapy and diagnosis, negative temperature coefficient of resistance, ferrofluids, high resistivity to corrosion, printing ink, magnetic resonance imaging, photoelectrodes for solar energy conversion and especially biomedical field [6,10–18]. Most of these functions depend strongly on the structure and morphology of the semiconductor materials, and one-dimensional (1D) α-Fe_2O_3 nanostructured material exhibits better electrochemical performance than that of bulk samples.

Up to now, a variety of α-Fe_2O_3 nanostructured materials in various geometrical morphologies have been successfully prepared, such as nanowires [19,20], nanocubes [21], nanoparticles [22], nanorods [23,24], nanobelts [25], nanorings [26], nanofibers [27], nanotubes [7,28], nanocages [29], nanoflakes [30] and complex hierarchical structures [31].

Su et al. synthesized hematite nanobelts and nanoflakes by oxidation of iron-coated ITO glass in air [32]. Esmaeili et al. used ferric-sugars, ferric-hydrazine and ferric-oleic acid as precursor to synthesize hematite nanoparticle via thermal treatment routes [33]. Jahangirdar et al. prepared α-Fe_2O_3 nanoparticles by a low temperature solution combination method [34]. α-Fe_2O_3 nanotubes have been synthesized by hydrothermal method by Song et al. [35]. Also, 3D urchin-like α-Fe_2O_3 nanostructure have been prepared by Sun et al. [36].

In this study, uniform α-Fe_2O_3 nanocrystals were synthesized by a simple hydrothermal process. The synthesis was performed in aqueous solution with the aid of organic ligand. The results of characterization showed that the product composed of α-Fe_2O_3 nanocrystals with the diameter of 40–50 nm.

*Tel./fax: +98 26 34551023.
E-mail address: mohammadikish@khu.ac.ir

0272-8842/$ - see front matter © 2013 Elsevier Ltd and Techna Group S.r.l. All rights reserved.
http://dx.doi.org/10.1016/j.ceramint.2013.07.016

2. Experimental

2.1. Materials and methods

All the chemicals were of analytical grade and were used as received without further purification.

X-ray diffraction patterns were recorded by a Rigaku D-max CIII, X-ray diffractometer using Ni-filtered Cu Ka radiation. Scanning Electron Microscopy (SEM) images were obtained on RMRC, VEGA TS 5136XM equipped with an energy dispersive X-ray spectroscopy. Transmission electron microscopy (TEM) images were obtained on a philips-cm10 ht-100 kV transmission electron microscope. Fourier transform infrared (FTIR) spectra were recorded on Rayleigh WQF-5 10 spectrophotometer in KBr pellets. The electronic spectra of the complexes were taken on a Bio UV–visible spectrometer (Varian Cary 100).

2.2. General procedure for the synthesis of α-Fe_2O_3 nanocrystals

In a typical synthesis, 2 mmol of salicylidene 2-aminophenol was dispersed in aqueous solution of 2 mmol sodium acetate. After 15 min stirring, an aqueous solution of 1 mmol of $Fe(NO_3)_3 \cdot 9H_2O$ was added. The yellow color of ligand solution changed to red immediately, which was then transferred into teflon lined stainless steel autoclave with 100 ml capacity, sealed and maintained at 110, 140, 160 and 180 °C for 24 h and at 140 °C for 6, 12 and 18 and 24 h. After the hydrothermal procedure, the autoclave cooled down to room temperature. The red precipitate was collected and repeatedly washed with distilled water and absolute ethanol and dried at 70 °C for 10 h.

3. Results and discussion

3.1. X-ray diffraction analysis

The crystallinity of the as-synthesized α-Fe_2O_3 was examined by XRD analysis. Fig. 1 shows the powder X-ray diffraction patterns of the resultant products obtained at different temperatures. All the diffraction peaks were readily indexed to a pure rhombohedral phase of α-Fe_2O_3 (JSPDS Card no. 24-0072) with $a=b=5.0380$ Å and $c=13.7720$ Å. The diffraction patterns are well matched with the literature [37] and no impurity peaks were observed. Furthermore, the strong and sharp diffraction peaks confirm the high crystallinity of the products.

It is known that line broadening of diffraction peaks is influenced by the crystallite size and the internal strains. The approximate crystallite size, d, can be evaluated using Scherrer's equation

$$d = k\lambda/\beta\cos\theta \quad (1)$$

where k is the so-called shape factor (0.9), λ is the wavelength (0.15418 nm, Cu Kα), β is the full width at half maximum (FWHM), and θ is the diffraction angle. From Scherrer's equation, the crystallite size of the nanoparticles at 160 and 180 °C were 37 and 44 nm, respectively.

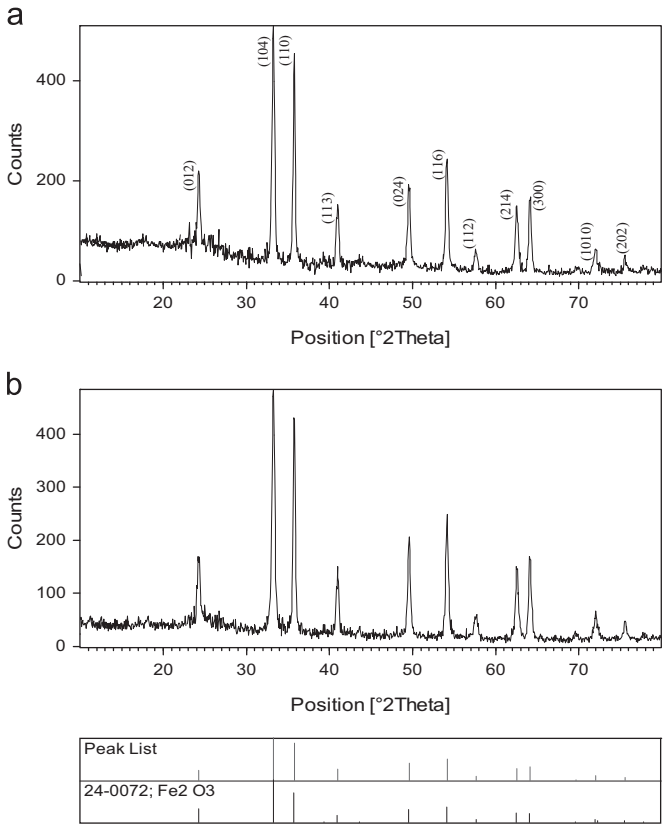

Fig. 1. XRD patterns of the as-prepared α-Fe_2O_3 samples at (a) 160 °C, and (b) 180 °C at 24 h.

The crystallinity and sizes of the resultant products were customarily enhanced by varying the reaction temperature. In higher temperature there is a significant grain growth and better crystallinity in comparison with lower temperatures.

3.2. Scanning electron microscopy

The morphologies and microstructures of the as-prepared products were illustrated by SEM observations. Figs. 2 and 3 show the detailed morphology of the hematite, from which weakly agglomerated α-Fe_2O_3 nanocrystals were clearly observed at different times and temperatures. As can be seen in the SEM images, nanostructures were in the form of nanocrystals with 40–50 nm in diameter. The agglomeration of nanocrystals is usually explained as a common way to minimize their surface free energy; however, some authors have reported that the agglomeration is assigned to the presence of organic radicals that act as binders [38].

3.3. Transmission electron microscopy

Fig. 4 displays the TEM images of the α-Fe_2O_3 nanoparticles. Most primary nanocrystals had ellipsoid shapes and completely discrete from each other, or connected together in some part of the samples. Agglomeration would occur when the TEM specimens were prepared by placing a small drop of

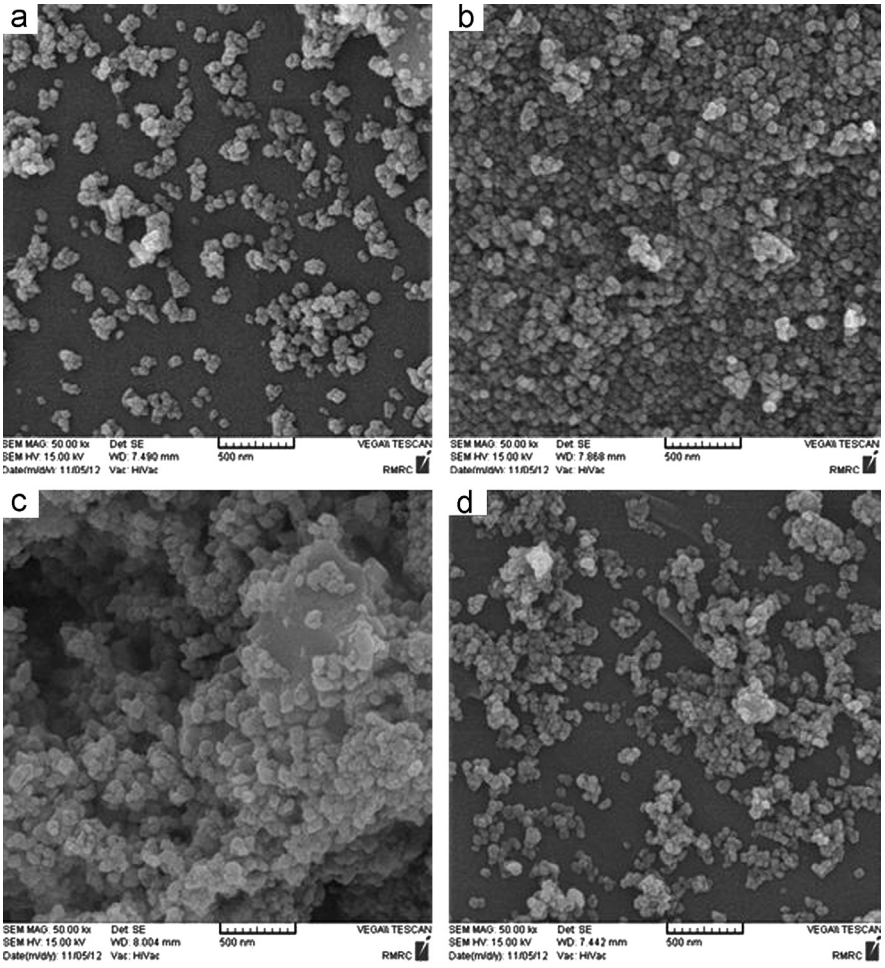

Fig. 2. SEM images of the as-prepared α-Fe_2O_3 samples at 140 °C for (a) 6 h, (b) 12 h, (c) 18 h and (d) 24 h.

the solutions onto a microgrid. The average diameter of the primary particles was 40–50 nm. The rombohedral crystalline structure of some particles can be seen clearly.

3.4. Formation mechanism

Prior to hydrothermal process, a FeL_n complex was formed by complexation of Fe(III) with Schiff base ligand that was derived from salicylaldehyde and 2-aminophenol. In the presence of CH_3COO^- the FeL_n complex was probably hydrolyzed to form FeOOH or $Fe(OH)_3$; and finally, the resulting FeOOH or $Fe(OH)_3$ decomposed into α-Fe_2O_3. During the hydrothermal process, some of the organic ligands would be dissociated from the Fe(III) and the newly formed Fe_2O_3 particles were partially capped with organic ligand. The formation of ellipsoid shape α-Fe_2O_3 based nanoparticles is most likely due to the fact that the formation of complexed Fe_2O_3 particles and the dissociation of organic ligand proceeded simultaneously during the hydrothermal process. The time-dependent morphology evolution study was conducted at 140 °C. The product obtained after 6 h is composed of spherical particles (Fig. 2a). Extending the reaction time to 12 h led to the agglomeration of the product (Fig. 2b). A mixture of ellipsoid and lozenge-like nanostructures was formed after 18 h (Fig. 2c). After 24 h, the less agglomerated nanostructures were obtained (Fig. 2d).

In addition to the reaction time, the effect of reaction temperature on the formation of the product was also studied at 24 h. At 110 °C, the agglomerated nanoparticles are formed (Fig. 3a). When the temperature was raised to 140 °C, some of the agglomerated particles were dissociated (Fig. 3b). At 160 °C ellipsoid particles are formed (Fig. 3c) that was more crystallized at 180 °C. Therefore, it clearly shows that increasing temperature and time can favor the formation of more crystalline nanostructures under the experimental conditions.

3.5. Fourier transform infrared spectroscopy

The formation of α-Fe_2O_3 nanoparticles was further confirmed by FT-IR spectroscopy. Fig. 5 shows FT-IR spectra of the as-formed α-Fe_2O_3 samples at different temperatures. The spectra show two characteristic bands of Fe–O at 465–474 and 548–555 cm^{-1}. The Fe–O frequencies of the samples prepared at 160 and 180 °C are sharper and stronger which show the better crystallinity of the nanostructures at higher temperature. The absorption bands at 3400 cm^{-1} are due to the presence of water. FT-IR spectra show that there is a small amount of capping agent (organic ligand) on the surface of as-prepared

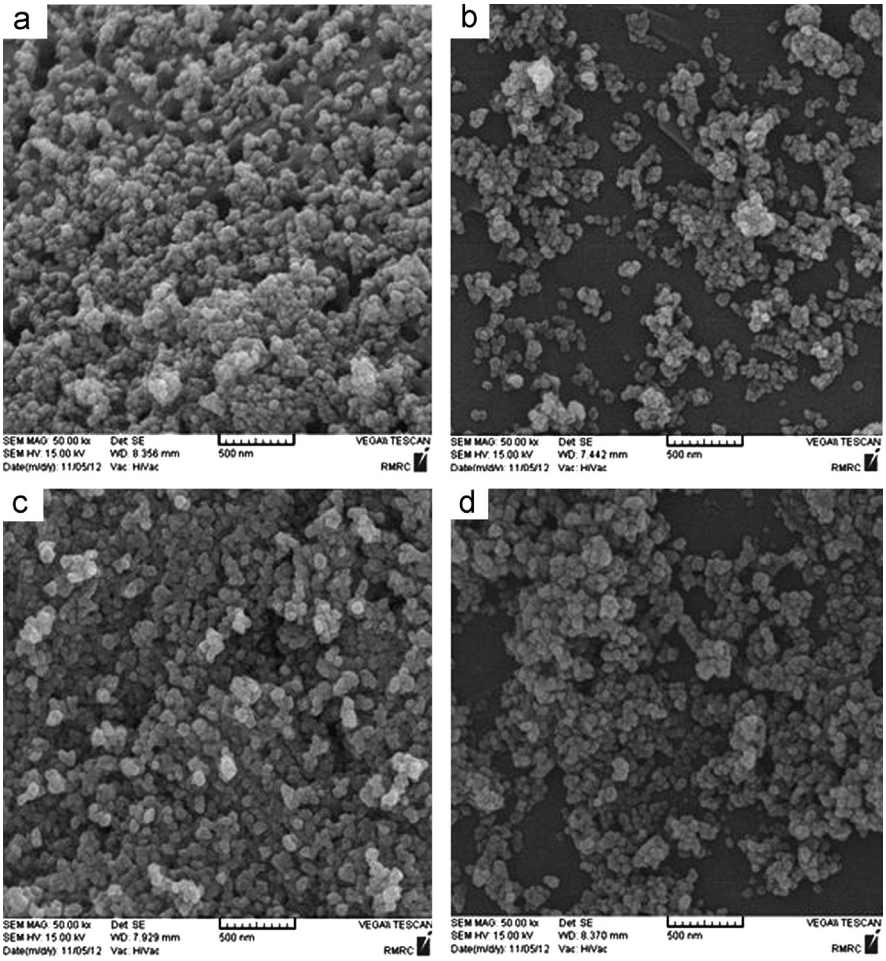

Fig. 3. SEM images of the as-prepared α-Fe_2O_3 samples at different temperatures: (a) 110 °C, (b) 140 °C, (c) 160 °C and (d) 180 °C for 24 h.

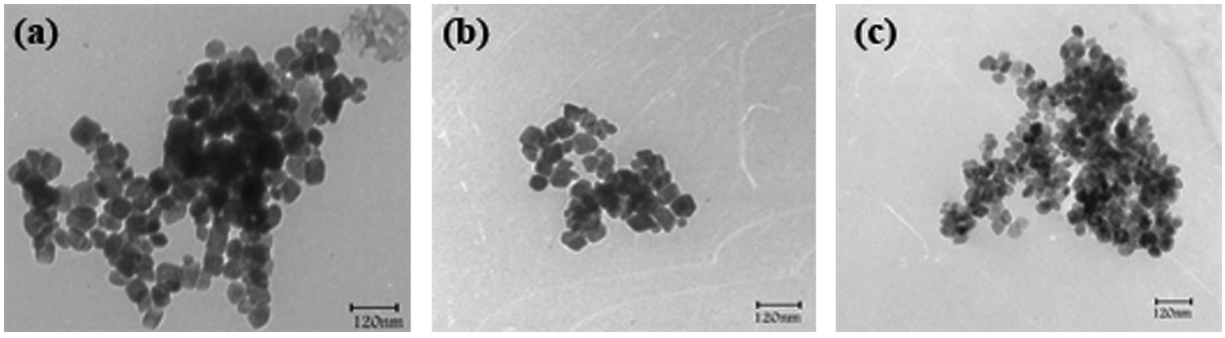

Fig. 4. TEM images of the as-prepared α-Fe_2O_3 samples at different temperatures: (a) 160 °C, (b) 160 °C, (c) 180 °C for 24 h.

products and confirm the stabilization of Fe_2O_3 nanoparticles. In the FT-IR spectra of the Fe_2O_3 samples, the CåN stretching frequencies at 1618 cm^{-1} did not change related to free ligand, this phenomena shows that the ligand does not coordinate to metal center and the connection may be due to adsorption or intermolecular interaction.

3.6. UV–vis spectroscopy and optical properties of α-Fe_2O_3

Nanostructured materials usually exhibit blue-shift phenomena in optical properties compared with the bulk counterparts. To reveal the electronic structure and size effect, UV–vis absorption measurement of the as-prepared α-Fe_2O_3 nanoparticles were carried out. According to the literature [39,40], two absorption regions are expected between 200 nm and 600 nm. The absorptions were observed at 200–300 nm centered at 270 nm (region 1) and at 400–600 nm with maximum about 540 nm (region 2) in Fig. 6. The first region mainly results from the ligand to metal charge transfer transitions and partly contributed from the Fe^{3+} ligand field transitions $^6A_1 \rightarrow {}^4T_1$ (^4P). In the second region the absorption peaks are mainly due to the $^6A_1 + {}^6A_1 \rightarrow {}^4T_1$ (^4G)+$^4T_1$ (^4G) excitation of an Fe^{3+}–Fe^{3+}

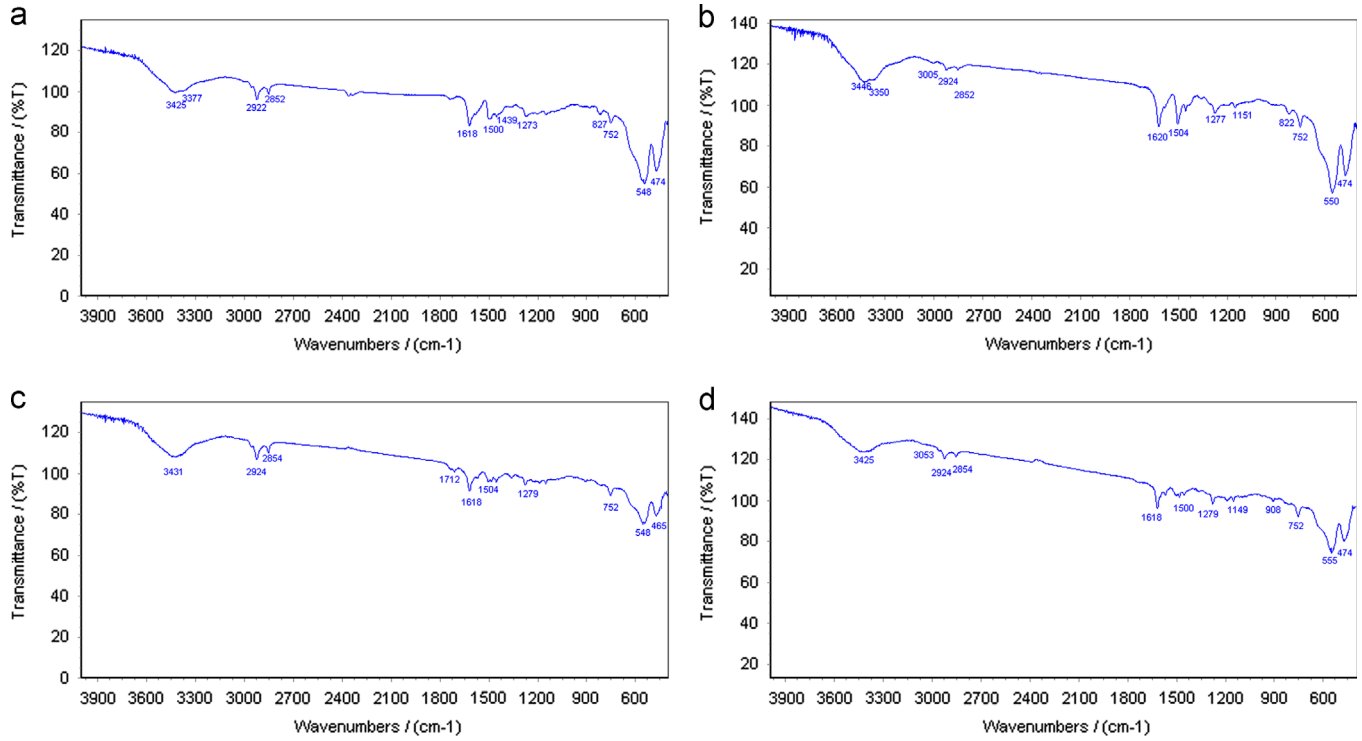

Fig. 5. FTIR spectrum of the as-prepared α-Fe_2O_3 samples at different temperatures: (a) 180 °C, (b) 160 °C, (c) 140 °C and (d) 110 °C for 24 h.

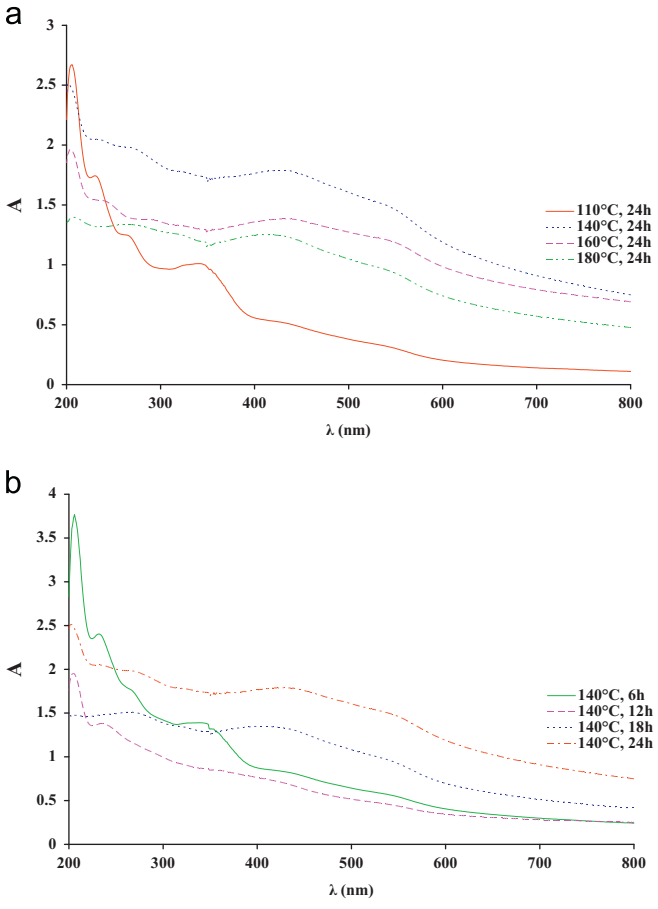

Fig. 6. UV–vis spectrum of the as-prepared α-Fe_2O_3 samples at (a) different temperatures and (b) different times.

pair, possibly overlapped with the contributions of $^6A_1 \rightarrow {}^4E$, $^4A_1$ (^4G) ligand field transition and the charge-transfer band tail. Xu et al. [41] reported similar results in α-Fe_2O_3 nano leaves synthesized by oxygenating pure iron. Further, Zhang et al. [42] reported the absorption spectrum of α-Fe_2O_3 nanoparticles suspended in ethanol. The absorption bands at 310 and 414 nm are assigned to the $^6A_1 \rightarrow {}^4T_1$ (^4P) and $^6A_1 \rightarrow {}^4T_2$ while the absorption bands in the visible region near 580 nm and 681 nm are assigned to the $^6A_1 + {}^6A_1 \rightarrow {}^4T_1$ (^4G)+$^4T_1$ (^4G) double exciton process (DEP) and $^6A_1 \rightarrow {}^4T_2$ (^4G) ligand field transitions of Fe^{3+} respectively.

It is a well-established fact that as a consequence of the quantum confinement of photogenerated electron-hole pairs, the UV–vis absorption spectra of semiconductor quantum dots is size dependent [43,44]. It is also noteworthy in this work that the absorption shoulder is red shifted with an increase in reaction temperature and time. This shows that crystal sizes increase with increasing reaction temperature; however, the SEM images of the products show that there is not a considerable change in the particle size of the nanospheres (Figs. 2 and 3). The direct band gap energy (E_g) of α-Fe_2O_3 nanoparticles was estimated using Tauc equation [45]

$$(\varepsilon h\nu) = C\left(h\nu - E_g\right)^n \quad (2)$$

where C is a constant, ε is the molar extinction coefficient, E_g is the average band gap of the material and n depends on the type of transition. The values of the molar extinction coefficients for the synthesized nanocrystals are more than 900; thus, we can assume that the transitions in the nanocrystals are allowed direct transitions. For $n = 1/2$, E_g in Eq. (2) is the

direct allowed band gap. The average band gap was estimated from the linear portion of the ($\varepsilon h\nu$) vs. $h\nu$ plots (Fig. 7) and was found to decrease with an increase in reaction temperature from 110–180 °C and reaction time from 6–24 h (Table 1). The band gap values were higher than that of bulk iron(III) oxide α-Fe_2O_3 (2.1 eV) due to the quantum confinement of α-Fe_2O_3 nanocrystals.

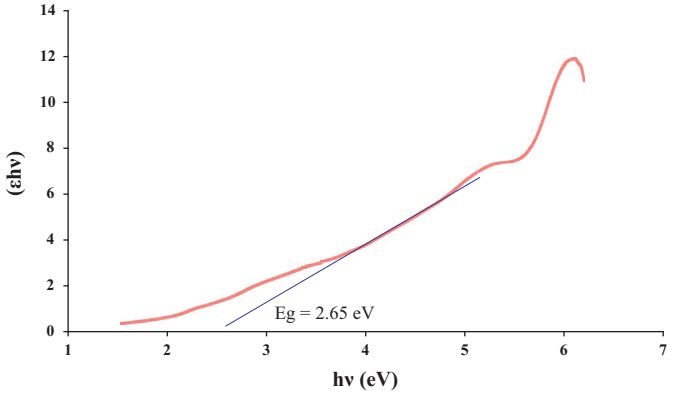

Fig. 7. Tauc plot of α-Fe_2O_3 at 140 °C and 12 h.

Table 1
Optical band gaps (E_g) of α-Fe_2O_3 samples at different temperatures and times.

	Time dependence at 140 °C				Temperature dependence at 24 h			
	6 h	12 h	18 h	24 h	110 °C	140 °C	160 °C	180 °C
E_g (eV)	2.7	2.65	2.60	2.55	2.75	2.55	2.50	2.3

3.7. The effect of sodium acetate

In addition to the reaction time and temperature, to elucidate the effect of sodium acetate some reaction was also carried out in the absence of this reagent. In the absence of sodium acetate, the FTIR spectra of the first sample, at 110 °C and 24 h (Fig. 8a), shows no Fe–O characteristic peak, but the vibrational frequencies of the Schiff base is sharper. When the reaction was carried out at 140 °C and 24 h (Fig. 8b), there is just some broadening in 400–500 cm^{-1} which is the characteristic region of Fe–O stretching vibrations. The XRD analysis confirms the formation of impure α-Fe_2O_3 (Fig. 9). In the XRD pattern, the diffraction peaks can be indexed as orthorhombic hematite but some amorphous solid was also

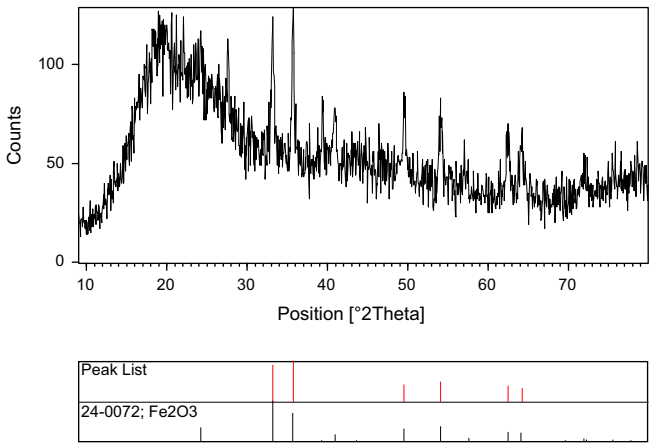

Fig. 9. XRD patterns of the impure α-Fe_2O_3 samples prepared in absence of sodium acetate at 140 °C and 24 h.

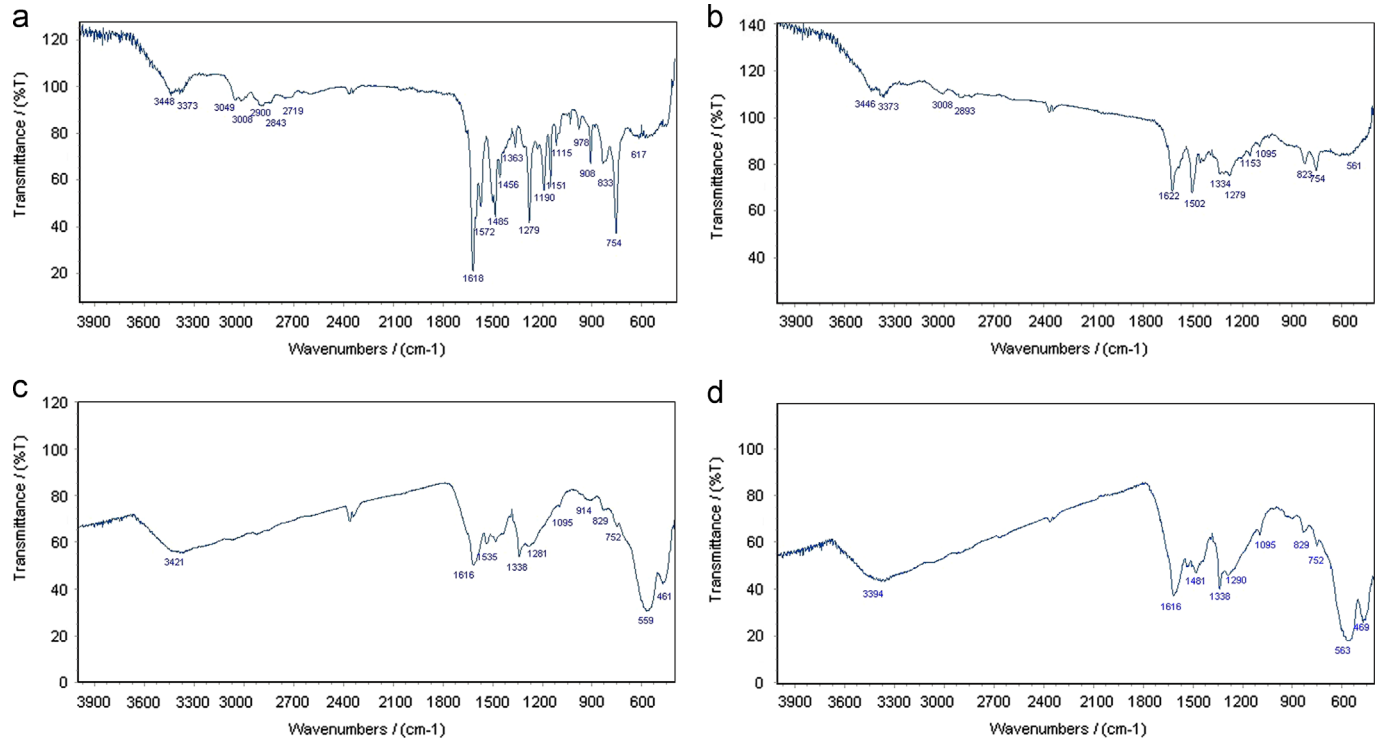

Fig. 8. FTIR spectra of the as-prepared α-Fe_2O_3 samples in absence of sodium acetate at: (a) 110 °C, 24 h (b) 140 °C, 24 h (c) 160 °C, 18 h (d) 180 °C 18 h.

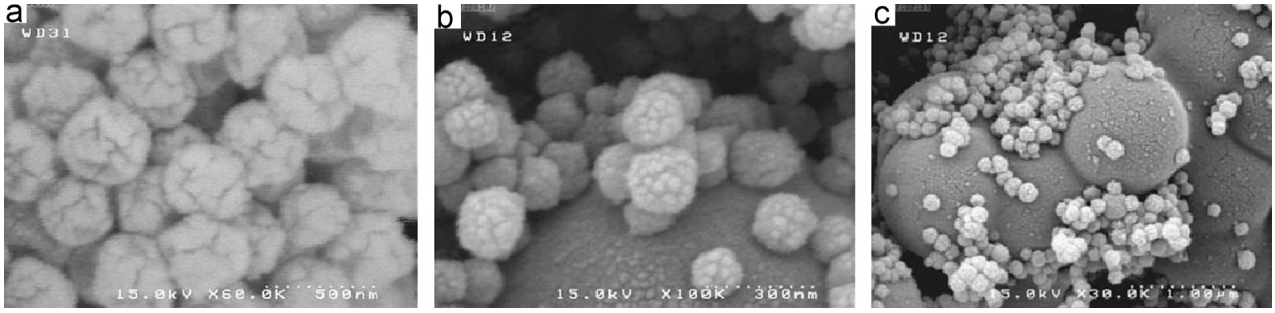

Fig. 10. SEM images of the as-prepared α-Fe_2O_3 samples prepared in absence of sodium acetate at (a) 140 °C, 24 h (b) 160 °C, 18 h (c) 180 °C 18 h.

observed. This experiment was done at 160 and 180 °C in 18 h without sodium acetate. The FTIR spectra (Fig. 8c and d) show two characteristic bands of Fe–O at 461–469 and 559–563 cm^{-1}. Therefore, it clearly shows that in the absence of sodium acetate, increasing temperature can favor the formation of α-Fe_2O_3 under the experimental conditions. SEM images of these samples are shown in Fig. 10. Here, in comparison with previous experiment in the presence of sodium acetate, more agglomeration can be observed.

4. Conclusion

In summary, hematite nanocrystals were successfully prepared and easily collected by a simple hydrothermal route in a one-step process. No γ-Fe_2O_3 phase was observed in the XRD patterns of the samples. TEM analysis showed that the particle size is controllable, with diameters about 40–50 nm. It has been found that the variations in reaction temperature and time have no significant effect on the shape and morphology of the α-Fe_2O_3 nanoparticles. However, the crystallite size of the as-produced material increases with increasing reaction temperatures and times. It is surprising to find that the pure sample of α-Fe_2O_3 nanoparticles cannot form in the absence of sodium acetate in lower temperatures.

References

[1] A.P. Alivisatos, Semiconductor clusters, nanocrystals, and quantum dots, Science 271 (1996) 933–937.
[2] V.L. Colvin, M.C. Schlamp, A.P. Alivisatos, Light-emitting diodes made from cadmium selenide nanocrystals and a semiconducting polymer, Nature 370 (1994) 354–357.
[3] R.M. Cornell, U. Schwertmann, The Iron Oxide, VCH, Weinheim, Germany, 1996.
[4] M.V. Kovalenko, M.I. Bodnarchuk, R.T. Lechner, G. Hesser, F. Schaffler, W. Heiss, Fatty acid salts as stabilizers in size- and shape-controlled nanocrystal synthesis: the case of inverse spinel iron oxide, Journal of the American Chemical Society 129 (2007) 6352–6353.
[5] Y.N. Li, P. Zhang, Z.P. Guo, Preparation of α-Fe_2O_3 submicro-flowers by a hydrothermal approach and their electrochemical performance in lithium-ion batteries, Electrochimica Acta 53 (2008) 4213–4218.
[6] J. Bandara, U. Klehm, W. Ki, Raschig rings-Fe_2O_3 composite photocatalyst activate in the degradation of 4-chlorophenol and Orange II under daylight irradiation, Applied Catalysis B: Environmental 76 (2007) 73–81.
[7] Z.Y. Sun, H.Q. Yuan, Z.M. Liu, B.X. Han, X.R. Zhang, A highly efficient chemical sensor material for H_2S: α-Fe_2O_3 nanotubes fabricated using carbon nanotube templates, Advanced Materials 17 (2005) 2993–2997.
[8] J. Chen, L.N. Xu, W.Y. Li, X.L. Gou, α-Fe_2O_3 nanotubes in gas sensor and lithium-ion battery applications, Advanced Materials 17 (2005) 582–586.
[9] A.S.S. Brown, J.S.J. Hargreaves, B. Rijniersce, A study of the structural and catalytic effects of sulfation on iron oxide catalysts prepared from goethite and ferrihydrite precursors for methane oxidation, Catalysis Letters 53 (1998) 7–13.
[10] S.W. Cao, Y.J. Zhu, Hierarchically nanostructured α-Fe_2O_3 hollow spheres: preparation, growth mechanism, photocatalytic property, and application in water treatment, Journal of Physical Chemistry C 112 (2008) 6253–6257.
[11] A. Kong, H.W. Wang, J. Li, Y.K. Shan, Preparation of super paramagnetic crystalline mesoporous γ-Fe_2O_3 with high surface, Materials Letters 62 (2008) 943–945.
[12] S.W. Cao, Y.J. Zhu, Surfactant-free preparation and drug release property of magnetic hollow core/shell hierarchical nanostructures, Journal of Physical Chemistry C 112 (2008) 12149–12156.
[13] V. Kesavan, P.S.S. Sivanand, Yu. Chandrasekaran, A. Koltypin, Gedanken, catalytic aerobic oxidation of cycloalkanes with nanostructured amorphous metals and alloys, Angewandte Chemie International Edition 38 (1999) 3521–3523.
[14] L.H. Huo, W. Li, L.H. Lu, H.N. Cui, S.Q. Xi, J. Wang, B. Zhao, Y.C. Shen, Z.H. Lu, Preparation, structure, and properties of three-dimensional ordered α-Fe_2O_3 nanoparticulate film, Chemistry of Materials 12 (2000) 790–794.
[15] K. Suresh, K.C. Patil, A combustion process for the instant synthesis of γ-iron oxide, Journal of Materials Science Letters 12 (1993) 572–574.
[16] M. Kroell, M. Pridoehl, G. Zimmermann, L. Pop, S. Odenbach, A. Hartwig, Magnetic and rheological characterization of novel ferrofluids, Journal of Magnetism and Magnetic Materials 289 (2005) 21–24.
[17] Y.S. Kang, S. Risbud, J.F. Rabolt, P. Stroeve, Synthesis and characterization of nanometer-size Fe_3O_4 and γ-Fe_2O_3particles, Chemistry of Materials 8 (1996) 2209–2211.
[18] S. Zhang, X.J. Chen, C.R. Gu, Y. Zhang, J.D. Xu, Z.P. Bian, D. Yang, N. Gu, The effect of iron oxide magnetic nanoparticles on smooth muscle cells, Nanoscale Research Letters 4 (2009) 70–77.
[19] Y.Y. Fu, R.M. Wang, J. Xu, J. Chen, Y. Yan, A.V. Narlikar, H. Zhang, Synthesis of large arrays of aligned α-Fe_2O_3 nanowires, Chemical Physics Letters 379 (2003) 373–379.
[20] R.M. Wang, Y.F. Chen, Y.Y. Fu, H. Zhang, C. Kisielowski, Bicrystalline hematite nanowires, Journal of Physical Chemistry B 109 (2005) 12245–12249.
[21] S.B. Wang, Y.L. Min, S.H. Yu, Synthesis and magnetic properties of uniform hematite nanocubes, Journal of Physical Chemistry C 111 (2007) 3551–3554.
[22] S. Giri, S. Samanta, S. Maji, S. Ganguli, A. Bhaumik, Magnetic properties of α-Fe_2O_3 nanoparticle synthesized by a new hydrothermal method, Journal of Magnetism and Magnetic Materials 285 (2005) 296–302.
[23] X. Wang, X. Chen, L. Gao, H. Zheng, M. Ji, C. Tang, T. Sen, Z. Zhang, Synthesis of β-FeOOH and α-Fe_2O_3 nanorods and electrochemical properties of β-FeOOH, Journal of Materials Chemistry 14 (2004) 905–907.
[24] K. Woo, H.J. Lee, J.P. Ahn, Y.S. Park, Sol–gel mediated synthesis of Fe_2O_3 nanorods, Advanced Materials 15 (2003) 1761–1764.
[25] X.G. Wen, S.H. Wang, Y. Ding, Z.L. Wang, S.H. Yang, Controlled growth of large-area, uniform, vertically aligned arrays of α-Fe_2O_3 nanobelts and nanowires, Journal of Physical Chemistry B 109 (2005) 215–220.

[26] X.L. Hu, J.C. Yu, J.M. Gong, Q.H. Li, α-Fe_2O_3 nanorings prepared by a microwave-assisted hydrothermal process and their sensing properties, Advanced Materials 19 (2007) 2324–2329.
[27] C.R. Gong, D.R. Chen, X.L. Xiao, Q.L. Wang, Continuous hollow α-Fe_2O_3 and α-Fe fibers prepared by the sol–gel method, Journal of Materials Chemistry 12 (2002) 1844–1867.
[28] C.J. Jia, L.D. Sun, Z.G. Yan, L.P. You, F. Luo, X.D. Han, Y.C. Pang, Z. Zhang, C.H. Yan, Single-crystalline iron oxide nanotubes, Angewandte Chemie International Edition 44 (2005) 4328–4333.
[29] D.B. Wang, C.X. Song, G.H. Gu, Z.S. Hu, Preparation of Fe_2O_3 microcages from the core/shell structures, Materials Letters 59 (2005) 782–785.
[30] M.V. Reddy, T. Yu, C.H. Sow, Z.X. Shen, C.T. Lim, G.V.S. Rao, B.V. R. Chowdari, α-Fe_2O_3 nanoflakes as an anode material for Li-ion batteries, Advanced Functional Materials 17 (2007) 2792–2799.
[31] K. He, C.Y. Xu, L. Zhen, W.Z. Shao, Fractal growth of single-crystal α-Fe_2O_3: from dendritic micro-pines to hexagonal micro-snowflakes, Materials Letters 62 (2008) 739–742.
[32] X. Su, C. Yu, C. Qiang, Synthesis of α-Fe_2O_3 nanobelts and nanoflakes by thermal oxidation and study to their magnetic properties, Applied Surface Science 257 (2011) 9014–9018.
[33] E. Esmaeili, M. Salavati-Niasari, F. Mohandes, F. Davar, H. Seyghalkar, Modified single-phase hematite nanoparticles via a facile approach for large-scale synthesis, Chemical Engineering Journal 170 (2011) 278–285.
[34] A.A. Jahagirdar, N. Dhananjaya, D.L. Monika, C.R. Kesavulu, H. Nagabhushana, S.C. Sharma, B.M. Nagabhushana, C. Shivakumara, J.L. Rao, R.P.S. Chakradhar, Structural, EPR, optical and magnetic properties of α-Fe_2O_3 nanoparticles, Spectrochimica Acta A 104 (2013) 512–518.
[35] L. Song, S. Zhang, B. Chen, J. Ge, X. Jia, A hydrothermal method for preparation of α-Fe_2O_3 nanotubes and their catalytic performance for thermal decomposition of ammonium perchlorate, Colloids and Surfaces A: Physicochemical Engineering Aspects 360 (2010) 1–5.
[36] P. Sun, W. Wang, Y. Liu, Y. Sun, J. Ma, G. Lu, Hydrothermal synthesis of 3D urchin-like α-Fe_2O_3 nanostructure for gas sensor, Sensors and Actuators B 173 (2012) 52–57.
[37] J. Hua, J. Gengsheng, Hydrothermal synthesis and characterization of monodisperse α-Fe_2O_3 nanoparticles, Materials Letters 63 (2009) 2725–2727.
[38] N. Dhananjaya, H. Nagabhushana, B.M. Nagabhushana, B. Rudraswamy, C. Shivakumara, R.P.S. Chakradhar, Effect of Li^+-ion on enhancement of photoluminescence in Gd_2O_3:Eu^{3+} nanophosphors prepared by combustion technique, Journal of Alloys and Compounds 509 (2011) 2368–2374.
[39] B.S. Zou, W. Huang, M.Y. Han, S.F.Y. Li, X.C. Wu, Y. Zhang, J. Zhang, J.S. Zhang, P.F. Wu, R.Y. Wang, Anomalous optical properties and electron-phonon coupling enhancement in Fe_2O_3 nanoparticles coated with a layer of stearates, Journal of Physics and Chemistry of Solids 58 (1997) 1315–1320.
[40] Y.P. He, Y.M. Miao, C.R. Li, S.Q. Wang, L. Cao, S.S. Xie, G.Z. Yang, B.S. Zou, C. Burda, Size and structure effect on optical transitions of iron oxide nanocrystals, Physical Review B 71 (2005) 125411–125419.
[41] Y.Y. Xu, D. Zhao, X.J. Zhang, W.T. Jin, P. Kashkarov, H. Zhang, Synthesis and characterization of single-crystalline α-Fe_2O_3 nanoleaves, Physica E 41 (2009) 806–811.
[42] G. Zhang, Y. Xu, D. Gao, Y. Sun, α-Fe_2O_3 nanoplates: PEG-600 assisted hydrothermal synthesis and formation mechanism, Journal of Alloys and Compounds 509 (2011) 885–893.
[43] L. Hu, J. Yan, M. Liao, H. Xiang, X. Gong, L. Zhang, X. Fang, An optimized ultraviolet-a light photodetector with wide-range photoresponse based on ZnS/ZnO biaxial nanobelt, Advanced Materials 24 (2012) 2305–2309.
[44] L. Hu, J. Yan, M. Liao, H. Xiang, X. Gong, L. Zhang, X. Fang, Multiangular branched ZnS nanostructures with needle-shaped tips: potential luminescent and field-emitter nanomaterial, Journal of Physical Chemistry C 112 (2008) 4735–4742.
[45] J. Tauc, in: F. Abeles (Ed.), Optical Properties of Solids, North-Holland, Amsterdam, 1970.